Electronic Supplementary Material (ESI) for Nanoscale.
This journal is © The Royal Society of Chemistry 2019

Polarization-dependent electric potential distribution across nanoscale ferroelectric $Hf_{0.5}Zr_{0.5}O_2$ in functional memory capacitors

Yury Matveyev[b,a*], *Vitalii Mikheev*[a], *Dmitry Negrov*[a], *Sergei Zarubin*[a], *Abinash Kumar*[c], *Everett D. Grimley*[c], *James M. LeBeau*[c], *Andrei Gloskovskii*[b], *Evgeny Y. Tsymbal*[d,a*] *and Andrei Zenkevich*[a*]

a) Moscow Institute of Physics and Technology, 9, Institutskiy lane, Dolgoprudny, Moscow region, 141700, Russia

b) Deutsches Elektronen-Synchrotron, 85 Notkestraße, Hamburg, D-22607, Germany

c) Department of Materials Science and Engineering, North Carolina State University, Raleigh, NC 27606, USA

d) Department of Physics and Astronomy, University of Nebraska-Lincoln, Lincoln, NE 68588, USA

* E-mails of corresponding authors: yury.matveev@desy.de; zenkevich.av@mipt.ru; tsymbal@unl.edu

S1 Sample growth procedure

Si (100) with native 2-nm-thick SiO_2 layer was used as a substrate. W layer ~50 nm in thickness was grown as a bottom electrode by magnetron sputtering. This layer was patterned by maskless optical lithography (Heidelberg Instruments μPG101) with SF_6 plasma etching (PlasmaLab System 100). Further, 9-nm thick $Hf_{0.5}Zr_{0.5}O_2$ (HZO) film was grown by atomic layer deposition in Sunale R-100 Picosun OY reactor at T=240°C using $Hf[N(CH_3)(C_2H_5)]_4$ (TEMAH), $Zr[N(CH_3)(C_2H_5)]_4$ (TEMAZ) and H_2O as precursors and N_2 as carrier and purge gas. The top TiN electrode was deposited at room temperature by magnetron sputtering. Since the maximal probing depth for HAXPES analysis at the X-ray energy E = 6 keV is ~ 20 nm, the thickness of the top TiN layer was chosen d ~ 10 nm to ensure both the continuous and conducting film, and sufficiently high yield of photoelectrons from the buried HZO layer.

In order to induce the crystallization of HZO layer in non-equilibrium ferroelectric phase, samples were exposed to rapid thermal annealing in Ar at T = 400°C for t = 1 min. The top electrodes were further patterned by maskless optical lithography (Heidelberg Instruments μPG101) with SF_6 plasma etching. To prevent any possible interaction of the TiN/HZO interface with plasma during the structure patterning [1,2,3], the active capacitor area was capped with a thick layer of resist (PMMA). At the same time, due to relatively large lateral dimensions of the

---

[1] S. Fang and J. P. McVittie, Thin-oxide damage from gate charging during plasma processing, IEEE Electron Device Letters 13, 288 (1992).

[2] C. D. Young, et al., Comparison of plasma-induced damage in SiO_2/TiN and HfO_2/TiN gate stacks, 2007 IEEE International Reliability Physics Symposium Proceedings, 45th Annual IEEE, 2007.

[3] P. J. Liao, et al., Physical origins of plasma damage and its process/gate area effects on high-k metal gate technology, 2013 IEEE International Reliability Physics Symposium (IRPS), IEEE, 2013.

capacitor structures, the effect of defects outside the active area on the electric field distribution across the ferroelectric layer inside the capacitor can be safely neglected.

In addition to the devices prepared for operando HAXPES with the lateral size 150x3000 μm^2, a set of small (150x150 μm^2) devices were patterned on the same chip for electrical pre-characterization of the sample.

Since the conductivity of the top ultrathin TiN electrode was rather limited, the contacts were made via Al paths and pads, deposited on the e-beam evaporated SiO_2 layer, also patterned by maskless optical lithography. The electrical contact to the common continuous bottom W electrode was made in form of two pads, formed at the sample corners by SF_6 plasma etching of all above layers and covered by Al.

S2 *In situ* electrical characterization of samples

For *in situ* switching of polarization and simultaneous measurements of I-V characteristics during HAXPES experiments, the two-channel Agilent B2912A source-meter unit was used. In all electrical measurements, the bottom electrode was grounded while the bias voltage was applied to the top electrode. In order to get rid of parasitic capacitance, the polarization current was measured at the bottom electrode.

The ferroelectric response of the capacitor devices was studied by the PUND (Positive Up Negative Down) technique. Typical voltage pulse train and current signals are shown in Figure S1. An input pulse train consists of two pairs of unipolar (positive and negative) trapezoidal pulses. We use the τ = 1.5 ms pulses with τ = 0.5 ms pulse edges. Such long pulses for operando experiments were selected in order to get rid of the distortion of the pulse shape while passing along the electrical line in and outside the UHV chamber due to the rather poor quality of the

transmission line (in particular, high RC value). During the first pulse in the pair of identical unipolar pulses, the current I_f is the sum of the current I_s associated with polarization switching and contributions not related to polarization switching, i.e. dielectric displacement, leakage and charge injection currents. The electric current during the second pulse has only the latter non-ferroelectric contributions. In this way, the polarization switching current I_p can be found as a difference between the integral current signals generated by the first and second unipolar pulses.

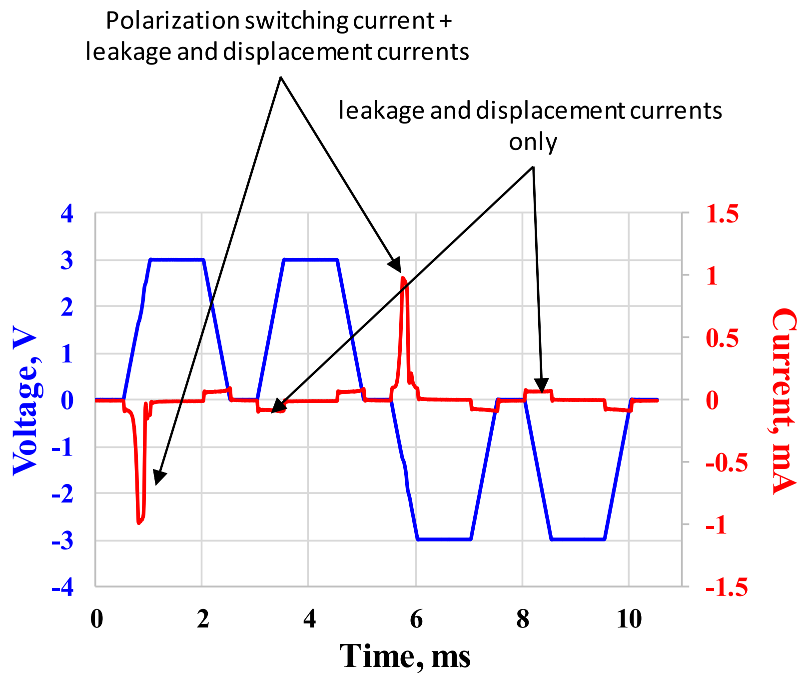

Figure S1. A typical in situ PUND voltage pulse train used for the pulsed switching testing and associated transient currents measured in the TiN/$Hf_{0.5}Zr_{0.5}O_2$/W capacitors.

In situ PUND measurements confirm that the polarization is maintained in the sample during acquisition of HAXPES spectra.

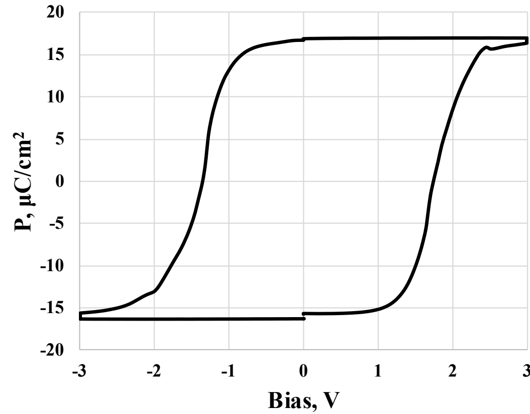

Figure S2. Polarization vs. voltage curve for a TiN/HZO/W ferroelectric capacitor as derived from in situ pulsed switching during HAXPES experiment.

The I-V curves measured prior to and approximately in the middle of HAXPES experiment (see Figure S3), do not show any increase of leakage current upon intense X-ray illumination of sample. Although these measurements cannot be considered as a comprehensive study of the X-ray effect on the device properties, they demonstrate that within the measured voltage range and duration of the experiment, X-rays do not produce any significant amount of defects in the HZO layer.

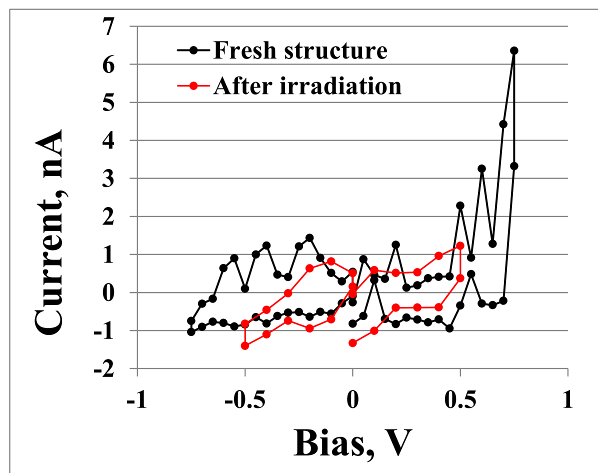

Figure S3: IV curves acquired before and in the middle of HAXPES measurements

In addition, the polarization value also maintains almost the same (see Figure S4). This can indicate that there is no detectable phase transition in HZO film during X-ray illumination.

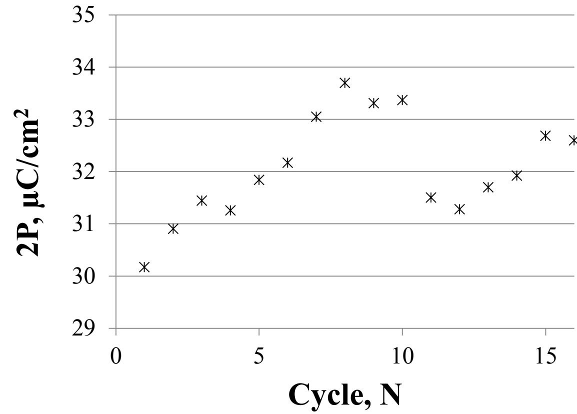

Figure S4: In situ measured polarization of the TiN/$Hf_{0.5}Zr_{0.5}O_2$/W capacitor as a function of cycle number during HAXPES experiment

S3 *Ex situ* electrical characterization of samples

The HAXPES measurements were performed at fully waked-up samples. The investigation of wake-up process was performed *ex situ* on the similar device on the same chip. *Ex situ* characterization of the fabricated TiN/$Hf_{0.5}Zr_{0.5}O_2$/W capacitor devices was performed using Cascade Summit 1100 probe station coupled with Agilent semiconductor device analyzer B1500A containing two B1530A waveform generator/fast measurement units and two source/measurement units connected via a selector. Figure S5 shows the typical behavior of polarization as a function of switching cycle, demonstration the practical absence of wake-up process in TiN/HZO/W structure. The larger polarization value compared to the sample measured *in situ* is attributed to the spread of polarization values for different capacitor devices on the chip.

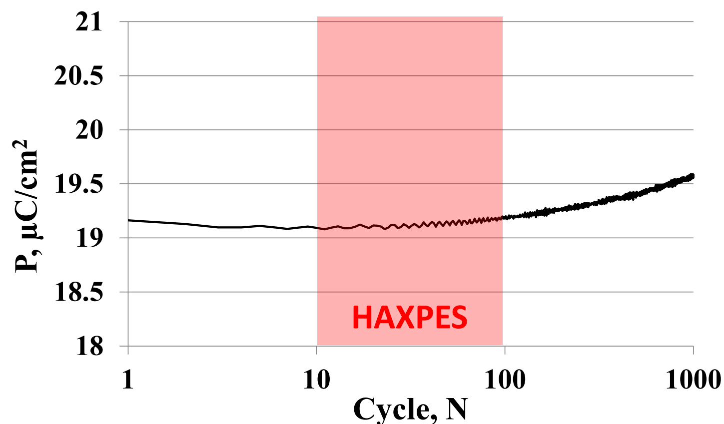

Figure S5: Measured polarization of the TiN/$Hf_{0.5}Zr_{0.5}O_2$/W capacitor as a function of the number of the switching cycles

S4 Effect of X-ray irradiation on the electronic structure of heterojunctions

Since the XPS is based on the photo effect, one should be aware of possible artifacts produced by the measurements (e.g. Refs. 4, 5). Indeed, only small part of the exited photoelectrons escape from the sample and is collected by analyzer. The rest are thermalized in the material and excite electron-hole pairs, which could contribute to the measured band lineup at the interface. Additionally, the X-ray could produce charged defects, which can also contribute to the measured band lineup. However, we have reasons to believe that these contributions are negligible and do not affect our measurements, as discussed below.

To monitor possible charging effects, we have performed two experiments. First, we measured the evolution of the Hf4$f_{7/2}$ peak position right away after switching the X-ray beam on. The X-rays incidence angle was chosen to be 0.5 degree, since at such an angle all the incoming X-rays are absorbed within the top 50 nm of our structure and we can obtain the

[4] J. R. Schwank, R. D. Nasby, S. L. Miller, M. S. Rodgers, and P. V. Dressendorfer, Total-dose radiation-induced degradation of thin film ferroelectric capacitors. IEEE Trans. Nucl. Sci. **37**, 1703 (1990).
[5] T. Tanimura, et al. "Analysis of x-ray irradiation effect in high-k gate dielectrics by time-dependent photoemission spectroscopy using synchrotron radiation." Surf. Interface Anal. **40**, 1606 (2008).

maximum flux of photoelectrons across the HZO layer. At such conditions, we can estimate the maximum amount of photoelectrons to be <$2 \cdot 10^{11}$ electrons/second. Even if we assume that all the photoelectrons are thermalized by producing the electron-hole pairs in HZO, we can produce maximum up to 10^{14} electrons. This value has the same order of magnitude as the estimated amount of defects in the HZO layer. As a result, if we again assume the ultimate case, i.e. all these electrons charge the defects, all the defects are going to be populated within 1 sec (at a full X-rays flux). For the beam attenuated N times, the specific charging time would increase to about N sec. This charging will inevitably produce the corresponding drift of the Hf4f peak position, since it changes the local potential in the HZO layer. However, as is evident from Figure S6, we did not observe any peak position drift with 4 different beam intensities: full flux, 14x, 50x and 200x times attenuated beam within first 10 min after switching the X-rays on.

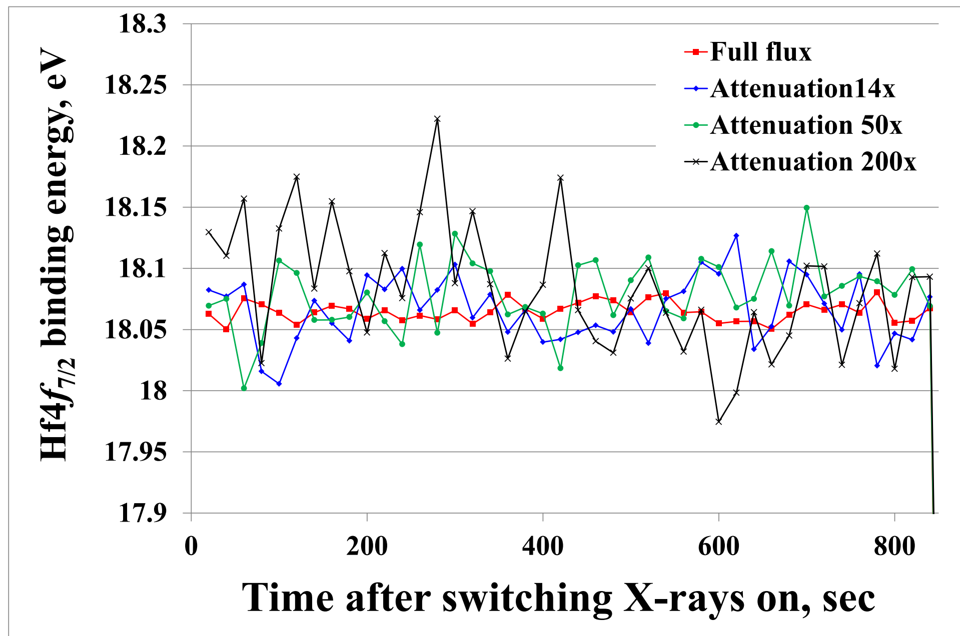

Figure S6. The evolution of the Hf4$f_{7/2}$ binding energy immediately after the switching the X-rays on as a function of the beam attenuation time

Second, we measured the position of the Hf4$f_{7/2}$, Hf3$d_{5/2}$ and Zr3$d_{5/2}$ spectral lines as a function of time for ~7 hours. The results are shown in Figure S7. It is seen that within the accuracy of measurements, there are no visible trends in changing the peak positions. Note that the relatively large dispersion (±0.05 eV) of the peak positions in Figures S6 and S7 is due to low statistics in the individual sweeps.

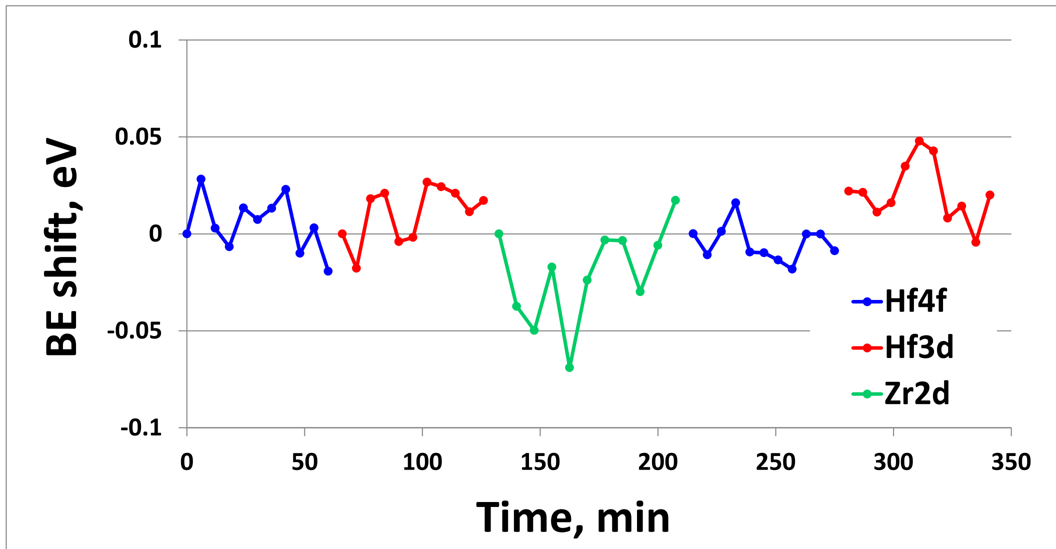

Figure S7. The shift of binding energy of Hf4f, Hf3d and Zr3d spectra lines in each sweep with respect to their initial value as a function of time (sweep number)

We can conclude therefore that there is no generation of charged defects during the experiment, which affect the results of our measurements.

S5 HAXPES spectra analysis

The distribution of both X-ray intensity and electrical potential across the HZO layer results in broadening, shift and attenuation/gain of the core-level lines spectra at different angles. Thus, the potential profile can be reconstructed from the collected spectra utilizing the following methodology.

S5.1 O1*s* spectral line

Fig. S8 (black line) shows the O1*s* core level spectrum measured on a device *in operando*. The detailed analysis of this spectrum appears to be difficult due to several reasons. First, in the samples prepared for *in-operando* measurements, the oxygen is present not only in the HZO layer, but also in the top TiN layer, in the partially oxidized Al electrode, surrounding the active area, and in the shielding SiO_2, which surrounds the active electrode. All these components lay on top of the HZO line and produce a signal about one order of magnitude stronger than that expected for the pristine HZO (blue line in Fig. S8). As a result, the O1*s* spectrum is broad (FWHM ~5 eV) and has quite complicated shape, from which it is impossible to reliably derive the shift of HZO component which is expected to be < 0.15 eV.

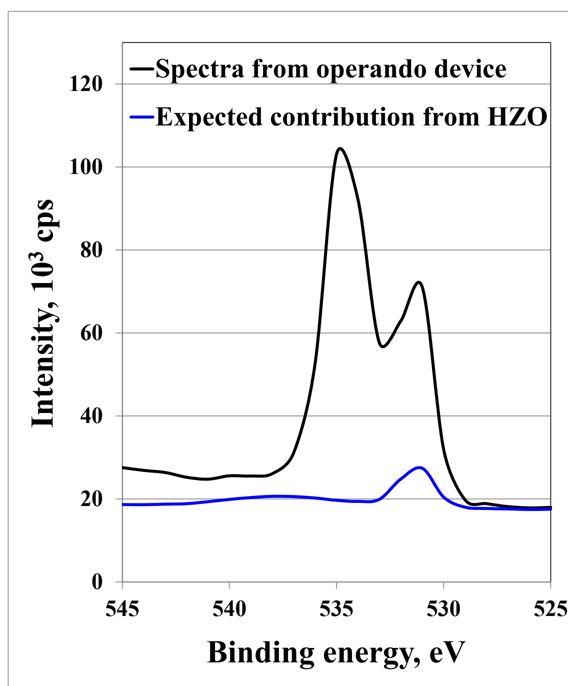

Figure S8: The O1s core level spectrum measured on a device in operando (black line) in comparison to the expected HZO spectrum (blue line).

In addition, our device structure has a 10 nm thick $Hf_{0.5}Zr_{0.5}O_2$ layer, of which 1 nm close to the top electrode and 2 nm close to the bottom electrode are defective. The total amount of oxygen atoms in the 10 nm HZO layer is $2.93 \cdot 10^{16}$ cm^{-2}. The amount of defects is ~$7 \cdot 10^{13}$ cm^{-2} and ~$6 \cdot 10^{13}$ cm^{-2} in the top and bottom defective layers, respectively, $1.3 \cdot 10^{14}$ cm^{-2} in total. That translates to $1.3 \cdot 10^{14} / 2.93 \cdot 10^{16} = 0.44\%$ of the total O concertation. Taking into account, that due to non-scattered photoelectrons, the signal from the bottom defective layer is attenuated by a factor of ~ 3, the "visible concentration" of oxygen vacancies is expected to be even lower (~0.3%). Such small changes are below the detection limit of XPS (>1-2%).

S5.2 Fitting the acquired HAXPES spectra

The experimental spectra were fitted using the UNIFIT 2017 software [6]. For the line shape, convolution of the Gauss and Lorentz distribution was taken, while for the background correction we utilized the Shirley background. As the result, the peak intensity, position and full width at half maxima were extracted from each spectrum and utilized for further analysis.

S5.3 Simulation of HAXPES line shape at particular angle

Each spectrum taken from FE-HZO sample at a particular angle was simulated as a sum of several components, representing virtual sub-layers in HZO. The required number of components was determined by additional simulations, which showed that in order to exclude any uncertainty one needs to use >100 sub-layers. In our case we used 201. Each component has its own binding energy shift proportional to the potential at the particular depth z, and the

[6] http://www.unifit-software.de

intensity is given by $I_{e^-} = I_{h\nu}(z) \cdot e^{-z/\lambda}$, where $I_{h\nu}(z)$ is X-ray intensity at the depth z, and λ is the effective attenuation length of photoelectrons in HZO (Figure S9).

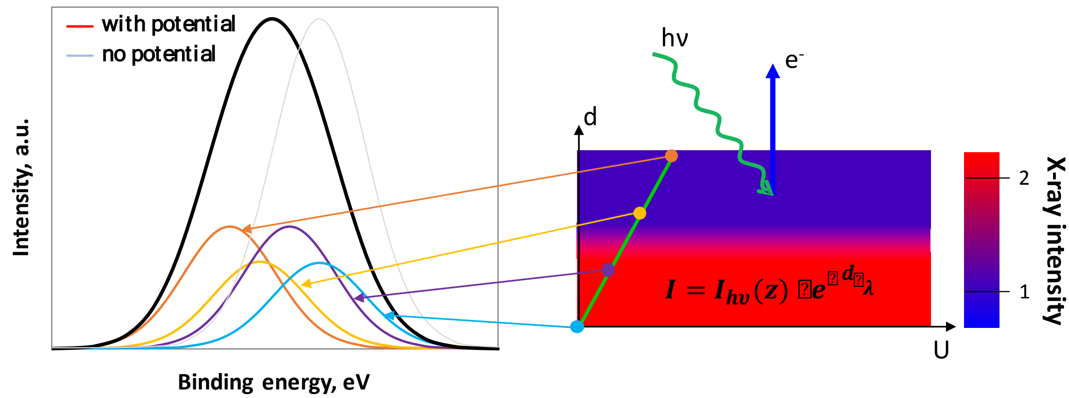

Figure S9: The schematic illustration of the core level spectra broadening arising from the distribution of potential and X-ray intensity in dielectric layer.

The simulated spectra were fitted by a line composed of convolution of a Gaussian and a Lorentzian, which allowed us to obtain the peak position, intensity and full width at half maximum.

S5.4 Fitting of X-rays intensity profile across the structure

In order to fit the obtained data, we first obtained the X-ray intensity profile across the sample as a function of the incident angle and then used the procedure similar to fitting XRR data. The only difference is that instead of reflected X-rays we analyzed the flux of photoelectrons, which is directly proportional to the X-ray absorption.

The X-ray intensity profiles were calculated by the TER_sl program at Sergey Stepanov's X-Ray Server [7, 8], which simulates the X-ray specular reflection from multilayers taking into

[7] X-Ray Server URL: http://x-server.gmca.aps.anl.gov

[8] S. Stepanov, "X-ray server: an online resource for simulations of X-ray diffraction and scattering". In:

account for interface roughness or transition layers. The initial values for each layer thickness and roughness of interfaces were determined from transmission electron microscopy cross-section images. The initial values of X-ray susceptibility were taken from the database X0h run by Sergey Stepanov.

The intensities of photoelectron peaks for each angle were calculated using the technique described in Section S3.2. For simplicity, we did not introduce any potential distribution at this stage, since the preliminary calculations showed that the presence of a reasonable potential distribution practically does not affect the shape of the intensity curve. Then each layer thickness, roughness and susceptibility coefficient were optimized in order to obtain the best matching of the measured and simulated values for the core-level peak intensities. The fitting was performed using a simple least squares procedure. The obtained X-ray intensity profile across the sample is shown in Figure 1b, while the experimental and fitted curves of the Hf4f7/2 peak intensity as a function of the X-ray incident angle are shown in Figure 2b. The exact parameters for each of the layers are collected in Table S1.

Table S1. The optimized parameters of each layer in TiN/HZO/W sample

	TiN	$Hf_{0.5}Zr_{0.5}O_2$	WO_x	W
Thickness, nm	9.1	9.6	3.1	56
Roughness, nm	0.6	0.9	0.9	0.7
X-ray susceptibility correction coefficient	1	1.3	1.5	1

S5.5 Fitting of the electric potential profile

"Advances in Computational Methods for X-ray and Neutron Optics", Ed. M.Sanches del Rio; Proceedings SPIE **5536**, 16-26 (2004).

The found $Hf4f_{7/2}$ peak intensity as a function of incident angle was used to obtain the electric potential profile. The shape of the potential was defined as a peace-wise linear function, and the fitting parameters were the positions of breakpoints and the potential values at these points, as illustrated in Figure S10. The positions of the breakpoints were assumed to be the same for both polarization directions.

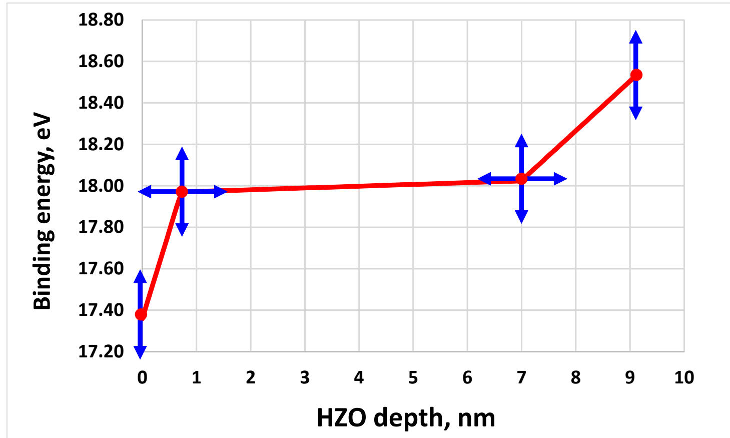

Figure S10: Illustration of the potential shape used for fitting. Arrows indicate degrees of freedom for the fitting parameters.

The number of breakpoints N in the model was optimized according to the Akaike information criterion (AIC), which provides an optimum solution as a function of model complexity (see Table S2).

Table S2 Residual sum of squares and AIC as a function of model complexity

# breakpoints, N	0	1	2	3
# fitting parameters, n	4	7	10	13
Residual sum of squares, $n \cdot 10^{-2}$	1.82	1.59	1.37	1.34
AIC value	-344	-350	**-357**	-353

The regions of confidence for each parameter were defined by t-test for each variable. The results of the fitting procedure show that the lowest AIC value is reached for N = 2, indicating

that the three-segment piecewise linear potential provides the optimal solution. For this potential profile, the obtained values of the Hf4$f_{7/2}$ core-level line binding energy at the interfaces and the breakpoints are summarized in Table S3.

Table S3 Hf4$f_{7/2}$ core-level line binding energy (in eV) at the interfaces and breakpoints of TiN/HZO/W devices for two opposite polarization directions.

	BE Hf4$f_{7/2}$, eV		
Breakpoint position, nm	Polarization		Up-Down difference
	Up	Down	
0	$17.90^{+0.12}_{-0.19}$	17.36 ± 0.05	0.55
0.8	18.07 ± 0.04	17.97 ± 0.03	0.1
7	18.05 ± 0.05	18.03 ± 0.02	0.02
9.1	$18.18^{+0.15}_{-0.05}$	18.55 ± 0.10	-0.38

S6 SW-HAXPES chemical profiling of TiN electrode

The measured Ti2*p* core-level spectra at different incident angles allows extracting the chemical profile across the TiN layer. In order to obtain this information, all the measured spectra were processed with the Unifit 2017 software. For the fitting, we utilized the Shirley background, while the peak shape was taken as the convolution of the Gaussian and Lorentzian lines. In order to accurately compare the TiN chemical states at the two interfaces, only the intensities of individual components were allowed to vary, while all the rest parameters (background shape, peak shape and position, doublet separation and ratio between components) were fixed. Figure 2a shows an example of fitting for the Ti2*p* line taken at angle 0.5 deg.

Using this approach, we analyzed the dependence of the TiN and TiO_x component intensities as a function of the X-ray incident angle. The results are shown in Figure S11, indicating an excellent agreement between the experimental and simulated data. In order to obtain the depth dependent intensities across the TiN layer, we used the same approach, as that

for the analysis of the HZO layer, but now assuming that the potential is constant across the TiN layer. Figure S12 shows the reconstructed chemical profile across the TiN layer. It is evident that there is a substantial fraction on the TiO_x component in the TiN layer within about 1 nm at the interface with HZO (smaller values of the TiN depth in Figure S12).

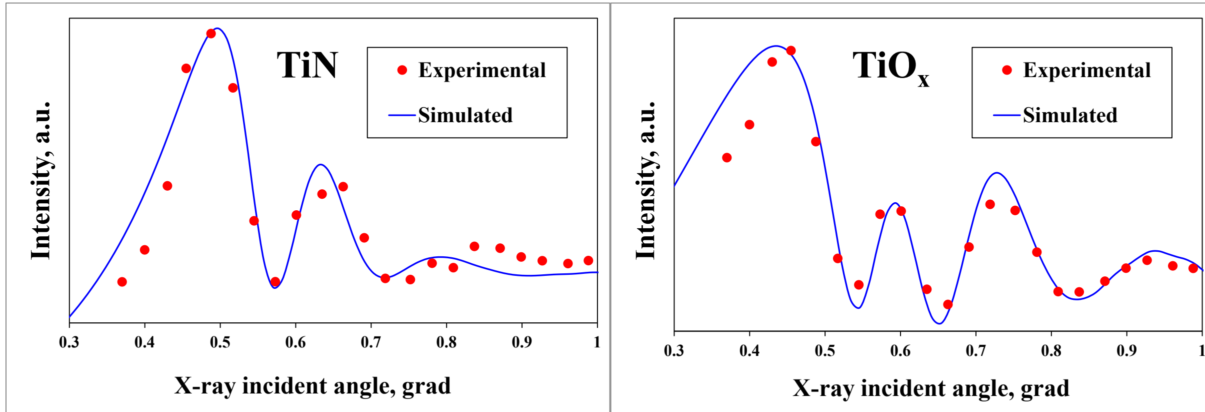

Figure S11. Measured and simulated intensities of the TiN and TiO_x components as a function of X-ray incident angle .

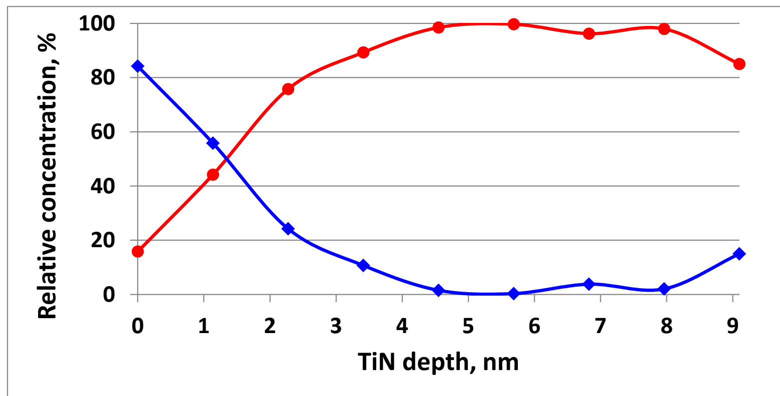

Figure S12. Depth profile of the TiN and TiO_x components in 9-nm-thick top TiN electrode reconstructed from the angular-dependent SW HAXPES data.

S7 Modelling of the electrical potential distribution

We assume that oxygen vacancies are formed and have constant total density N_V within a layer of thickness l_V in HZO adjacent to the top TiN/HZO interface, as shown by the brown line in Figure 3b of the main text. Within this layer, the oxygen vacancies can be neutral (V^0), single charged (V^+), and double charged (V^{++}). Their respective concentrations, N_{V^0}, N_{V^+}, and $N_{V^{++}}$, are depth-dependent, but the sum is constant so that

$$N_V = N_{V^0} + N_{V^+} + N_{V^{++}} \quad . \tag{1}$$

The neutral oxygen vacancy, which is the void on an oxygen site filled with two electrons, does not change the overall electric potential. In contrast, the charged oxygen vacancy lowers the potential energy and thus increases the probability for the oxygen vacancy site to be filled with an electron tunnelling from the electrode. The probability for oxygen vacancy of being neutral or charged is described by the Fermi-Dirac statistics.

The concentration of neutral oxygen vacancies is given by:

$$N_{V^0} = N_V \left(\frac{1}{\exp\left((E_{CB} - E_V)/k_B T \right) + 1} \right)^2 , \tag{2}$$

which accounts for the probability for two electrons to occupy the vacancy site. Here E_{CB} is the depth-dependent conduction band energy derived from the experiment (dashed line in Figure 3b), E_V is the energy of the V^0 energy level with respect to the conduction band edge.

Similarly, the concentration of single-charged oxygen vacancies is given by:

$$N_{V^+} = N_V \frac{1}{\exp\left((E_{CB} - E_V)/k_B T \right) + 1} - N_{V^0} \quad .$$

(3)

In Eqs. (2) and (3), we assume for simplicity that E_V is independent of the oxygen vacancy charge state. The space charge created by oxygen vacancies can be expressed as:

$$\rho_V = 2eN_{V^{++}} + eN_{V^{+}}, \tag{4}$$

where $N_{V^{++}} = N_V - N_{V^0} - N_{V^+}$.

We assume further that there are defects in HZO within a layer l_D adjacent to the bottom HZO/W interface. These defects have constant total density N_D (brown line in Figure 3b of the main text) and can be neutral (D^0) or negatively charged (D^-). Their respective concentrations, N_{D^0} and N_{D^-}, are depth-dependent, but the sum is constant so that

$$N_D = N_{D^0} + N_{D^-}. \tag{5}$$

The negatively charged defects are filled with electrons and create an electric potential, which enhances the probability of an electron to tunnel into the W electrode leaving the defect site empty. The concentration of the charged defects is given by:

$$N_{D^-} = N_D \frac{1}{\exp\left((E_{CB} - E_D)/k_B T\right) + 1}, \tag{6}$$

where E_D is the energy level of the defect with respect to the conduction band edge. The space charge created by the charged defects is:

$$\rho_D = -eN_{D^-}. \tag{7}$$

The electric potential φ across the HZO layer is given by the Poisson equation:

$$\frac{\partial^2 \varphi}{\partial z^2} = -\frac{(\rho_V + \rho_D)}{\varepsilon \varepsilon_0}.$$

(8)

The electric potential shifts locally the conduction band energy E_{CB} and thus affects the number of charged/neutral oxygen vacancies and defects at the top and bottom interfaces, thus defining the space charge distribution. We solve the Poisson equation (8) numerically, using for the boundary conditions the experimentally derived CBO values at the TiN/HZO and HZO/W interfaces.

Using l_V, N_V, E_V, l_D, N_D, and E_D as fitting parameters, we fit then the calculated potential profile to the potential derived from the experiment. The fitting is performed by minimization of the objective function given by:

$$f(l_V, N_V, E_V, l_D, N_D, E_D) = \int_0^d \frac{(\varphi(z) - \varphi_{exp}(z))^2 dz}{\sigma^2} , \qquad (9)$$

where d is the HZO layer thickness, $\varphi(z)$ is the modelled electric potential for given values of l_V, N_V, E_V, l_D, N_D, and E_D, $\varphi_{exp}(z)$ is the experimentally derived electric potential profile for a given polarization direction, and σ^2 is the variance estimated from the experimental results.

The resulting distribution of charged oxygen vacancies and defects in the top and bottom interface layers for both polarization orientations is presented in Figure S13.

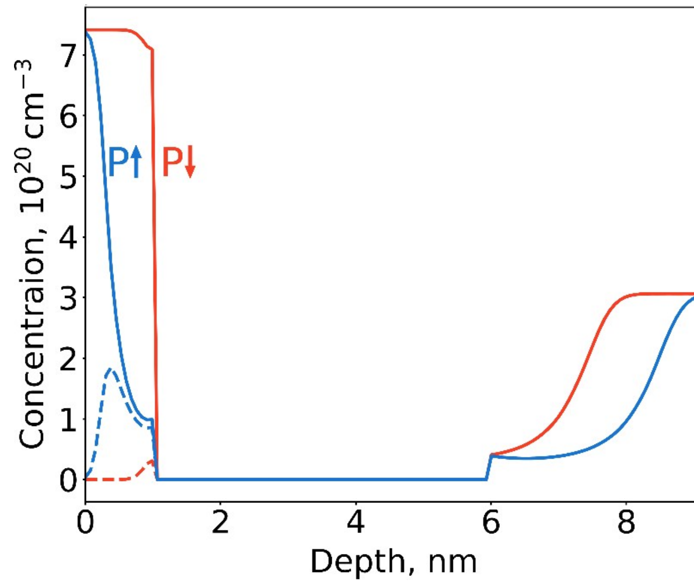

Figure S13. The modelled concentration of positively double-charged (solid lines) / single-charged (dashed lines) oxygen vacancies and negatively charged defects close to the top and bottom HZO interface, respectively, for polarization up (blue) and down (red).